

P3MaZe: a Mass-Zero constrained-dynamics formulation of particle–mesh electrostatics

Federica Troni¹, Violette Gontran¹, Davide Grassano¹, and Sara Bonella^{*1,2}

¹Centre Européen de Calcul Atomique et Moléculaire (CECAM), Ecole Polytechnique Fédérale de Lausanne, 1015 Lausanne, Switzerland

²National Centre for Computational Design and Discovery of Novel Materials (MARVEL), Ecole Polytechnique Fédérale de Lausanne, CH-1015 Lausanne, Switzerland

*Email: sara.bonella@epfl.ch

Abstract

We introduce P3MaZe, a real-space particle–mesh electrostatic method that combines the standard short-range/long-range decomposition of Particle-Particle Particle-Mesh (P3M) electrostatics with the Mass-Zero constrained dynamics (MaZe) framework. In this formulation, the smooth long-range electrostatic potential is represented on a mesh as a zero-inertia auxiliary field, while the discretized Poisson equation is enforced as a holonomic constraint during molecular dynamics. By retaining the standard P3M decomposition, P3MaZe preserves the systematic accuracy controls associated with the real-space cutoff, the Ewald splitting, the mesh spacing, and the charge-assignment procedure, while replacing the conventional multigrid Poisson solver by a constrained correction problem. The method is validated for molten NaCl and simple point-charge flexible water (SPC/Fw). Structural, translational, collective, and rotational dynamical observables are in quantitative agreement with those obtained with established electrostatic methods, including real-space P3M, and Ewald summation. The constrained formulation consistently requires fewer multigrid iterations than the corresponding real-space P3M solver while retaining the expected linear scaling with system size. These results establish P3MaZe as a promising new direction for scalable real-space electrostatics in large-scale molecular simulations.

Keywords

Real–space particle–mesh electrostatics; Constrained dynamics; Molecular dynamics.

Introduction

The evaluation of long-range electrostatic interactions remains one of the main challenges in large-scale classical molecular dynamics (MD) simulations. Unlike short-ranged van der Waals interactions, these interactions cannot be treated by a simple local truncation in a controlled manner [1]. Under periodic boundary conditions (PBC), the lattice sum is conditionally convergent, and the electrostatic response contains both a singular short-range component, dominated by local pairwise interactions, and a long-range component that remains collective over the periodic system [2]. Highly efficient methods have been developed to address this problem and are now routinely employed in molecular simulations [3]. Nevertheless, when simulations scale to millions of degrees of freedom, as required for realistic modelling of complex biophysical and materials systems, long-range electrostatics continues to be one of the dominant computational bottlenecks [4, 5]. On modern heterogeneous many-core and GPU architectures, this cost is increasingly dominated by communication rather than arithmetic operations, motivating the development of algorithms with improved communication locality [6–8].

The separation of length scales in the electrostatic response is at the heart of state-of-the-art algorithms that treat the short- and long-range components with different numerical approaches. This strategy forms the basis of Ewald-type methods and their particle-mesh variants [9]. In Ewald summation, the Coulomb interaction is decomposed into a short-range contribution, evaluated by direct pair summation in real space, and a smooth long-range contribution, evaluated analytically in reciprocal space [10]. Particle-mesh methods, including Particle Mesh Ewald [11, 12] and P3M [13], retain the Ewald short/long decomposition but accelerate the smooth long-range calculation by solving it numerically. In reciprocal space, the discretized Poisson equation becomes diagonal and can therefore be solved efficiently using three-dimensional Fast Fourier transform (FFT). The accuracy of these methods can be systematically controlled through the real-space cutoff, the Ewald splitting parameter, the mesh spacing, and the charge-assignment order, which together determine the balance between real-space truncation error and mesh/discretization error. Particle-mesh methods combine systematic control of electrostatic accuracy with excellent computational efficiency and have consequently become the standard approach for large-scale molecular simulations. Although substantial effort has been devoted to improving the scalability of distributed FFT implementations in modern molecular simulation packages [14–16], the associated three-dimensional FFTs require global communication patterns that still limit scalability [5–7].

Attempts to improve long-range solvers can be broadly divided into two classes: methods that avoid FFTs by adopting a different electrostatic formulation, and methods that retain the particle-mesh decomposition but replace the FFT-based mesh solver by a real-space one. The first class includes, for example, fast multipole and tree-based methods, that replace the particle-mesh solve by hierarchical expansions of distant charge distributions [17–19]. This can provide favorable scaling, but the accuracy is controlled by expansion order, clustering criteria, and the treatment of periodic images, rather than by the standard P3M parameters of splitting, mesh spacing, and charge assignment. A different approach is provided by multilevel summation methods. These retain a separation between local interactions and smooth corrections, but the long-range contribution is distributed over a hierarchy of grids, leading to a different interpolation and error structure from a single P3M mesh solve [20, 21]. An alternative strategy is adopted by local-field methods, such as those introduced by Maggs and Rossetto, which reformulate electrostatics in terms of locally evolving electric fields satisfying Gauss’s law [22, 23]. These methods eliminate global FFTs but depart from the standard particle-mesh decomposition and therefore adopt a fundamentally different numerical framework. Finally, more local alternatives (e.g. damped or shifted pairwise approximations) modify the Coulomb potential itself, thus avoiding a global solve. The quality of these approximation depends, however, on the system and on the observables considered [24].

For the present work, the relevant route is the second one: retaining the P3M short/long decomposition and its associated error controls, while replacing the FFT-based mesh solve by a real-space solver. Within the class of P3M-based methods, Beckers *et al.* employed successive over-relaxation to solve the discretized Poisson equation on a real-space grid [25], while Sagui and Darden adopted a multigrid solver [26], achieving linear scaling with the number of particles and grid points. Related ideas have also been developed for non-periodic systems. In particular, Sutmann and Steffen proposed a particle-particle particle-multigrid method in which the near-field contribution is evaluated explicitly and the far-field contribution is obtained from a multigrid Poisson solver with boundary conditions determined by a multipole expansion [27]. These approaches demonstrate that replacing the FFT-based mesh solve is compatible with retaining the particle-mesh decomposition and its systematic accuracy control, motivating the search for more efficient real-space formulations.

In this paper, we introduce P3MaZe, a MaZe formulation of particle-mesh electrostatics. The MaZe formalism promotes appropriate auxiliary quantities, typically featuring as parameters subjected to conditions in the evolution of physical degrees of freedom, to zero-inertia dynamical variables whose values are determined by enforcing appropriate holonomic constraints during the dynamics. In this way, repeated solution of auxiliary optimization or field equations is replaced by constrained dynamical evolution while preserving the desired equilibrium distribution.

The MaZe approach stems from an original formulation proposed by Ciccotti and Ryckaert to describe rotation-translation coupling in diatomic molecules [28]. Over the past few years, it has been revived and generalized to a broad range of problems, including classical polarizable models [29, 30], constant-potential electrochemical simulations [31], shell models in magnetic fields [32], orbital-free first-principles MD [33], and advanced classical simulations of supercapacitors [34].

In very recent work [35], the MaZe formalism was applied to the solution of electrostatic interactions under the name Poisson MaZe. In Poisson MaZe, the electrostatic potential on a real-space grid is represented by zero-inertia auxiliary variables, while the discretized Poisson equation is enforced as a holonomic constraint. An efficient multigrid constraint solver yields linear scaling with the number of degrees of freedom and requires fewer iterations than conventional multigrid Poisson solvers. The formulation also preserves key physical properties, including energy and momentum conservation, time reversibility, and stationarity of ensemble averages. However, Poisson MaZe treats the full Coulomb problem on the grid. Consequently, the fine spatial resolution required to represent the short-range electrostatic potential must be maintained throughout the simulation domain, increasing both the number of auxiliary variables and the size of the constrained problem.

The present work overcomes these limitations by combining the systematic accuracy framework of particle–mesh electrostatics with the MaZe constrained-dynamics formalism. In P3MaZe, the short-range contribution is evaluated by conventional particle–particle summation, while only the smooth long-range mesh potential is represented by zero-inertia auxiliary variables. The corresponding mesh equation is enforced as a holonomic constraint at every time step, replacing the conventional FFT-based reciprocal-space solve by a local constrained solver. The method preserves systematic control of accuracy. We assess it by comparing structural and dynamical observables for molten NaCl and SPC/Fw water against reference Poisson MaZe, P3M and Ewald calculations, and conducting a detailed analysis of computational performance.

Theory

Consider a system of N_p point particles with coordinates $\{\mathbf{r}_\beta\}$, masses $\{m_\beta\}$, and charges $\{Q_\beta\}$. The corresponding microscopic charge density is

$$\rho(\mathbf{r}) = \sum_{\beta=1}^{N_p} Q_\beta \delta(\mathbf{r} - \mathbf{r}_\beta). \quad (1)$$

Under periodic boundary conditions, the electrostatic energy includes the interaction of each charge with all of its periodic replicas and is given by

$$V_c = \frac{1}{2} \sum_{\mathbf{n} \in \mathbb{Z}^3} \sum_{\alpha=1}^{N_p} \sum_{\beta=1}^{N_p} \frac{Q_\alpha Q_\beta}{|\mathbf{r}_{\alpha\beta} + \mathbf{n}_{\text{cell}}|}, \quad (2)$$

where $\mathbf{r}_{\alpha\beta} = \mathbf{r}_\alpha - \mathbf{r}_\beta$, $\mathbf{n}_{\text{cell}} = n_1 \mathbf{a}_1 + n_2 \mathbf{a}_2 + n_3 \mathbf{a}_3$ is a lattice vector of the simulation cell, and the prime excludes the singular self interaction $\alpha = \beta$ for $\mathbf{n}_{\text{cell}} = \mathbf{0}$. The lattice sum is conditionally convergent and is defined according to the usual Ewald convention [1]. Following the standard particle–mesh formulation [13], the periodic Coulomb interaction is decomposed into a rapidly decaying short-range contribution and a smooth long-range contribution by introducing a screening charge density associated with each particle. The total screening density is

$$\rho^s(\mathbf{r}) = \sum_{\beta=1}^{N_p} \rho_\beta^s(\mathbf{r}; \{\mathbf{r}_\beta\}), \quad (3)$$

In the present work we adopt Gaussian screening functions,

$$\rho_\beta^s(\mathbf{r}; \{\mathbf{r}_\beta\}) = \frac{Q_\beta}{(2\pi\sigma^2)^{3/2}} \exp\left[-\frac{|\mathbf{r} - \mathbf{r}_\beta|^2}{2\sigma^2}\right], \quad (4)$$

consistent with the formulation of Beckers [25]. The electrostatic energy is written, exactly, as

$$V_c = V_{\text{SR}} + V_{\text{LR}} + V_{\text{self}}. \quad (5)$$

With our choice for the screening density, the short-range contribution - given by the difference between the Coulomb interaction of the point charges and that of the corresponding screening densities - is,

$$\begin{aligned} V_{\text{SR}} &= \frac{1}{2} \sum_{\mathbf{n} \in \mathbb{Z}^3} \sum_{\alpha=1}^{N_p} \sum_{\beta=1}^{N_p} \left[\frac{Q_\alpha Q_\beta}{|\mathbf{r}_{\alpha\beta} + \mathbf{n}_{\text{cell}}|} - \int d\mathbf{r} d\mathbf{r}' \frac{\rho_\alpha^s(\mathbf{r}; \{\mathbf{r}_\alpha\}) \rho_\beta^s(\mathbf{r}'; \{\mathbf{r}_\beta\})}{|\mathbf{r} - \mathbf{r}' + \mathbf{n}_{\text{cell}}|} \right] \\ &= \frac{1}{2} \sum_{\alpha=1}^{N_p} \sum_{\beta \neq \alpha}^{N_p} \frac{Q_\alpha Q_\beta}{r_{\alpha\beta}} \left[1 - \text{erf} \left(\frac{r_{\alpha\beta}}{\sqrt{2}\sigma} \right) \right]. \end{aligned} \quad (6)$$

This term decays rapidly and is evaluated only for particle pairs within a real-space cutoff R_c . The term

$$\begin{aligned} V_{\text{self}} &= -\frac{1}{2} \sum_{\alpha=1}^{N_p} \int d\mathbf{r} d\mathbf{r}' \frac{\rho_\alpha^s(\mathbf{r}; \{\mathbf{r}_\alpha\}) \rho_\alpha^s(\mathbf{r}'; \{\mathbf{r}_\alpha\})}{|\mathbf{r} - \mathbf{r}'|} \\ &= -\frac{1}{\sqrt{2\pi}\sigma} \sum_{\alpha=1}^{N_p} Q_\alpha^2. \end{aligned} \quad (7)$$

removes the self interaction of each screening density.

The smooth long-range interaction is

$$V_{\text{LR}} = \frac{1}{2} \sum_{\mathbf{n} \in \mathbb{Z}^3} \sum_{\alpha=1}^{N_p} \sum_{\beta=1}^{N_p} \int d\mathbf{r} d\mathbf{r}' \frac{\rho_\alpha^s(\mathbf{r}; \{\mathbf{r}_\alpha\}) \rho_\beta^s(\mathbf{r}'; \{\mathbf{r}_\beta\})}{|\mathbf{r} - \mathbf{r}' + \mathbf{n}_{\text{cell}}|}, \quad (8)$$

which retains the full periodic long-range electrostatic contribution. Rather than evaluating Eq. (8) directly, particle-mesh methods determine the corresponding electrostatic potential by solving the Poisson equation

$$\nabla^2 \phi_{\text{LR}}(\mathbf{r}) = -4\pi \rho^s(\mathbf{r}), \quad (9)$$

which, after discretization on a uniform grid of spacing h , becomes

$$\mathbf{M} \phi_{\text{LR}} = -4\pi \frac{\mathbf{q}^s}{h}, \quad (10)$$

where \mathbf{M}/h^2 is the discrete Laplacian and \mathbf{q}^s/h^3 is the vector of assigned smooth charges. Up to this point, the formulation of the problem follows the standard particle-mesh formulation. The remaining numerical task is the solution of the discrete Poisson equation at every simulation step. Conventional particle-mesh methods perform this solve using either FFT-based reciprocal-space techniques or iterative real-space solvers. The novel, key, idea that P3MaZe brings in is to reformulate the long-range particle-mesh problem as a constrained dynamical system. Instead of solving the discrete Poisson equation Eq. (10) at every molecular dynamics step, the values of the long-range electrostatic potential on the mesh are promoted to auxiliary dynamical variables. The discrete Poisson equation is then enforced as a holonomic constraint within the MaZe formalism, following the approach previously developed for Poisson MaZe [35].

To this end, the components of the discretized long-range electrostatic potential, ϕ_{LR} , are assigned a finite auxiliary inertia μ (whose vanishing limit will be considered below), leading to the extended Lagrangian

$$\begin{aligned} \mathcal{L}_{\text{P3MaZe}} &= \frac{1}{2} \sum_{\beta=1}^{N_p} m_\beta \dot{\mathbf{r}}_\beta^T \dot{\mathbf{r}}_\beta + \frac{1}{2} \mu \dot{\phi}_{\text{LR}}^T \dot{\phi}_{\text{LR}} \\ &\quad - \bar{V}(\{\mathbf{r}_\beta\}) - V_{\text{SR}}(\{\mathbf{r}_\beta\}) - V_{\text{LR}}(\phi_{\text{LR}}; \{\mathbf{r}_\beta\}) - V_{\text{self}} - \boldsymbol{\lambda}^T \boldsymbol{\sigma}_{\text{LR}}(\phi_{\text{LR}}; \{\mathbf{r}_\beta\}), \end{aligned} \quad (11)$$

where $\bar{V}(\{\mathbf{r}_\beta\})$ contains all non-electrostatic interactions and $\boldsymbol{\lambda}$ denotes the vector of Lagrange multipliers associated with the constraints. The discretized long-range electrostatic energy is

$$V_{\text{LR}}(\phi_{\text{LR}}; \{\mathbf{r}_\beta\}) = \frac{h}{8\pi} \phi_{\text{LR}}^T \mathbf{M} \phi_{\text{LR}} + \phi_{\text{LR}}^T \mathbf{q}^s, \quad (12)$$

and the holonomic constraints are defined as the stationarity conditions of the long-range energy,

$$\begin{aligned}\boldsymbol{\sigma}_{\text{LR}}(\boldsymbol{\phi}_{\text{LR}}; \{\mathbf{r}_{\beta}\}) &= \nabla_{\boldsymbol{\phi}_{\text{LR}}^T} V_{\text{LR}}(\boldsymbol{\phi}_{\text{LR}}; \{\mathbf{r}_{\beta}\}) \\ &= \frac{h}{4\pi} \mathbf{M} \boldsymbol{\phi}_{\text{LR}} + \mathbf{q}^s(\{\mathbf{r}_{\beta}\}) = \mathbf{0}.\end{aligned}\tag{13}$$

Eq. (13) is exactly the discrete Poisson equation (Eq. (10)) expressed as a holonomic constraint. Consequently, the constraint manifold coincides with the set of mesh potentials satisfying the discrete Poisson equation. Furthermore, when the constraint is satisfied,

$$V_{\text{LR}} = \frac{1}{2} \boldsymbol{\phi}_{\text{LR}}^T \mathbf{q}^s,\tag{14}$$

which is the standard discrete expression for the electrostatic energy of the smooth charge distribution.¹ The evolution equations for the extended system follow from the Euler–Lagrange equations. As in the general MaZe formalism [29, 35], the physical dynamics are recovered in the limit $\mu \rightarrow 0$. In this limit, the Lagrange multipliers scale linearly with μ , ensuring that the acceleration of the auxiliary variables remains finite. As shown in the Supporting Information, the resulting equations of motion are

$$\begin{aligned}m_{\alpha} \ddot{\mathbf{r}}_{\alpha} &= \nabla_{\mathbf{r}_{\alpha}} V_{\text{SR}}(\{\mathbf{r}_{\beta}\}) - \nabla_{\mathbf{r}_{\alpha}} V_{\text{LR}}(\boldsymbol{\phi}; \{\mathbf{r}_{\beta}\}) - \nabla_{\mathbf{r}_{\alpha}} \bar{V}(\{\mathbf{r}_{\beta}\}), \\ \ddot{\boldsymbol{\phi}}_{\text{LR}} &= -\mathbf{M} \boldsymbol{\eta},\end{aligned}\tag{15}$$

where $\boldsymbol{\eta} = \lim_{\mu \rightarrow 0} \frac{h}{4\pi} \frac{\boldsymbol{\lambda}}{\mu}$ is the rescaled vector of Lagrange multipliers.

In practice, the physical degrees of freedom are propagated using the velocity–Verlet algorithm, while the auxiliary variables are integrated using the Verlet scheme. At each time step, the rescaled Lagrange multipliers are determined by enforcing the constraint $\boldsymbol{\sigma}_{\text{LR}}(\boldsymbol{\phi}_{\text{LR}}; \{\mathbf{r}_{\beta}\}) = \mathbf{0}$, via an adapted SHAKE algorithm [36]. Thus, the dynamics evolve directly on the constraint manifold defined by Eq. (13), ensuring that the mesh potential remains consistent with the smooth charge density throughout the simulation.

P3MaZe and P3M: Correction problem vs Poisson solver. The P3MaZe formulation shares the same particle–mesh decomposition as conventional real-space P3M methods and therefore determines the same long-range electrostatic potential. The essential difference lies in the numerical problem solved at each molecular dynamics step. In a conventional real-space P3M method, the mesh potential is obtained by directly solving the discretized Poisson equation (Eq. (10)) at every molecular dynamics step. In P3MaZe, by contrast, the mesh potential is propagated as an auxiliary dynamical variable using a Verlet step, after which the discrete Poisson equation is enforced through the SHAKE correction. Denoting by $\boldsymbol{\phi}_{\text{LR},p}^{k+1} = 2\boldsymbol{\phi}_{\text{LR},p}^k - \boldsymbol{\phi}_{\text{LR},p}^{k-1}$ the Verlet prediction of the long-range potential at time step $(k+1)$, the constraint correction is obtained by solving

$$\mathbf{M} \mathbf{y} = \boldsymbol{\sigma}_{\text{LR},p}^{k+1},\tag{16}$$

where $\mathbf{y} = \frac{h}{4\pi} \frac{\Delta t^2}{2} \mathbf{M} \boldsymbol{\eta}$ is proportional to the rescaled Lagrange multiplier (Eq. (15)). The right-hand side is the residual associated with the predicted field,

$$\boldsymbol{\sigma}_{\text{LR},p}^{k+1} = \frac{h}{4\pi} \mathbf{M} \boldsymbol{\phi}_{\text{LR},p}^{k+1} + \mathbf{q}^{s,k+1}.\tag{17}$$

Thus, unlike conventional real-space P3M methods, P3MaZe does not solve the Poisson equation for the electrostatic potential itself. Instead, it solves the correction problem required to project the dynamically predicted potential onto the constraint manifold defined by Eq. (13). This reformulation is inherited from the original Poisson MaZe method [35].

An important consequence is that the iterative solver benefits from two high-quality initial guesses: the predicted mesh potential produced by the Verlet step and the predicted Lagrange multiplier. The latter

¹Eq. (14) is the discrete counterpart of $V_{\text{LR}} = \frac{1}{2} \int_{\Omega} d\mathbf{r} \rho^s(\mathbf{r}) \phi_{\text{LR}}(\mathbf{r})$, equivalent to the Green-function representation in Eq. (8).

can be given by the multiplier inherited from the previous time step or by more effective predictors, as detailed in the results. A conventional Poisson solver has access to neither quantity. As demonstrated for Poisson MaZe [35], these additional predictors substantially reduce the number of multigrid iterations required for convergence. The same advantage is retained in P3MaZe while preserving the standard particle–mesh decomposition. Its impact on convergence and overall computational performance is quantified in the Results Section.

P3MaZe and Poisson MaZe: Charge assignment and smoothing. An important distinction between Poisson MaZe and P3MaZe concerns the source term of the mesh Poisson equation. In Poisson MaZe, the full particle charge density is assigned directly to the grid and acts as the source of the discretized Poisson problem. In P3MaZe, by contrast, the source term is the smooth screening charge density arising from the particle–mesh decomposition, as in conventional real-space P3M methods [25, 26]. Consequently, P3MaZe inherits the systematic accuracy framework of particle–mesh electrostatics. In the present implementation, particle charges are first assigned to the mesh using cubic B-splines. The resulting charge density is subsequently smoothed over a finite stencil to obtain the mesh density \mathbf{q}^s entering Eq. (13). Because the source term is smooth, the corresponding mesh potential is also smoother than in Poisson MaZe, with reduced high-frequency components of the mesh potential. This in turn reduces the mesh resolution required to achieve a given target accuracy and therefore the number of necessary auxiliary variables. This additional smoothing operation introduces an extra particle–mesh cost that is absent in Poisson MaZe. As shown below, however, this overhead is more than compensated by the reduced cost of the constrained mesh solver, leading to an overall improvement in computational efficiency.

P3MaZe and Poisson MaZe: Electrostatic energy. The particle–mesh decomposition also simplifies the evaluation of the electrostatic energy. In Poisson MaZe, the electrostatic potential is obtained from the full discretized Poisson problem, so a direct evaluation of the mesh energy contains a grid self-energy associated with the discrete representation of each particle charge [13, 35]. This contribution depends on both the charge-assignment scheme and the mesh resolution, making its removal numerically delicate. For this reason, Poisson MaZe evaluates the electrostatic energy from the mechanical work performed by the electrostatic forces along the trajectory,

$$V_c^{\text{work}}(t) = - \sum_{\alpha=1}^{N_p} \int_{\mathbf{r}_\alpha^0}^{\mathbf{r}_\alpha(t)} \mathbf{F}_\alpha \cdot d\mathbf{r}_\alpha. \quad (18)$$

rather than directly from the mesh variables.

In P3MaZe, this complication disappears naturally. The electrostatic energy is evaluated from the standard particle–mesh decomposition (Eq. (5)). The mesh contributes only through the smooth long-range energy V_{LR} (Eq. (7)), while the singular Coulomb interaction is treated analytically by V_{SR} . Consequently, the grid self-energy associated with the discretized point charges is absent. The only remaining self contribution is the analytical Gaussian screening correction (Eq. (6)).

Electrostatic forces. The electrostatic force follows the same decomposition as the energy,

$$\mathbf{F}_\alpha = \mathbf{F}_\alpha^{\text{SR}} + \mathbf{F}_\alpha^{\text{LR}}, \quad (19)$$

where the short-range contribution is evaluated analytically. For the Gaussian screening function (Eq. (4)),

$$\mathbf{F}_\alpha^{\text{SR}} = \sum_{\substack{\beta \neq \alpha \\ r_{\alpha\beta} < R_c}} Q_\alpha Q_\beta \left[\frac{\text{erfc}(r_{\alpha\beta}/\sqrt{2}\sigma)}{r_{\alpha\beta}^3} + \sqrt{\frac{2}{\pi}} \frac{\exp[-r_{\alpha\beta}^2/(2\sigma^2)]}{\sigma r_{\alpha\beta}^2} \right] \mathbf{r}_{\alpha\beta}, \quad (20)$$

where $\mathbf{r}_{\alpha\beta} = \mathbf{r}_\alpha - \mathbf{r}_\beta$, ($r_{\alpha\beta} = |\mathbf{r}_{\alpha\beta}|$), and the sum is restricted to particle pairs within the real-space cutoff R_c .

The long-range contribution is obtained from the constrained mesh potential using the same interpolation procedure employed in Poisson MaZe. For example, the (x)-component is

$$F_{\alpha,x}^{\text{LR}} = -Q_{\alpha} \sum_n W(\mathbf{r}_{\alpha} - \mathbf{r}_n) D_x \phi_{\text{LR},n}, \quad (21)$$

where D_x denotes the finite-difference approximation to the mesh gradient and W is the particle–mesh interpolation function. Greek subscripts label particles, whereas Latin subscripts denote mesh points. In the present implementation, W is a cubic B-spline, identical to the charge-assignment function. Using the same interpolation function for charge assignment and force reconstruction ensures consistency between the two operations, as in Poisson MaZe.

The P3MaZe force construction preserves the momentum-conserving properties of both components of the particle–mesh decomposition. The short-range contribution is pairwise and antisymmetric and therefore conserves total momentum exactly (up to floating-point roundoff). As in Poisson MaZe, the long-range contribution conserves momentum on the mesh provided that charge assignment and force interpolation employ the same weight function and the Laplacian is discretized using central finite differences [13]. In the present implementation, both conditions are satisfied by using cubic B-splines together with the standard seven-point finite-difference stencil. Higher-order Hermitian discretizations [26] could be adopted straightforwardly if greater mesh accuracy were required.

Taken together, these differences show that P3MaZe combines the systematic accuracy and analytical structure of particle–mesh electrostatics with the constrained-dynamics formulation and efficient iterative correction strategy of Poisson MaZe.

Results

Molten salt

System and simulation protocol

As a first validation of the method, we consider molten NaCl, which provides a direct comparison with our previous Poisson MaZe formulation [35]. Since P3MaZe differs from Poisson MaZe only in the treatment of the long-range electrostatic problem, this system allows us to isolate the effect of introducing the particle–mesh decomposition while keeping the underlying constrained-dynamics framework unchanged.

The simulated system consists of 250 ions (125 Na^+ and 125 Cl^-) in a cubic simulation cell of side $L = 20.64 \text{ \AA}$, corresponding to a density of $1.3793 \text{ g} \cdot \text{cm}^{-3}$. Periodic boundary conditions are applied in all directions. Non-electrostatic interactions are described by the Born–Huggins–Meyer potential with Tosi–Fumi parameters, following the model adopted in previous simulations of molten NaCl [35, 37, 38].

Initial configurations were generated from a bcc lattice with Maxwell–Boltzmann velocities at $T = 1550 \text{ K}$. After equilibration in the canonical ensemble using Langevin dynamics integrated with the OVRVO splitting scheme [39], production trajectories were generated in the microcanonical ensemble by setting the friction coefficient to zero, thereby recovering the velocity–Verlet limit. The equilibration stage lasted 2.5 ps with a time step of 0.25 fs. For P3MaZe, the electrostatic parameters were chosen according to the convergence analysis reported in the Supporting Information. The Gaussian screening width was set to $\sigma = 1.39 \text{ \AA}$, corresponding to an Ewald splitting parameter $\beta = 0.5087 \text{ \AA}^{-1}$, the real-space cutoff was $R_c = 4.5 \text{ \AA}$, and the mesh consisted of 60^3 grid points ($h = 0.344 \text{ \AA}$). The smooth charge density was generated using the diffusion-based smoothing procedure of Beckers and co-workers [25, 26], whose computational cost scales linearly with the number of mesh points. For comparison, Poisson MaZe calculations employed the optimized setup of Ref. [35], using a 120^3 mesh ($h = 0.172 \text{ \AA}$). In both methods, the constraint equations were solved at every molecular dynamics step to a tolerance of 10^{-7} .

Structural and dynamical validation

The purpose of the following analysis is to establish that replacing the full-grid Poisson formulation of Poisson MaZe by the particle–mesh decomposition of P3MaZe preserves both equilibrium and dynamical properties. We therefore compare structural, single-particle transport, and collective transport observables obtained with the two methods against available literature data.

The equilibrium liquid structure is first assessed through the partial radial distribution functions. Fig. 1 compares the Na–Cl, Na–Na and Cl–Cl distributions obtained from 25 ps microcanonical trajectories with those reported by Galamba *et al.* [37]. The P3MaZe and Poisson MaZe curves are indistinguishable within graphical resolution for all ionic pairs, demonstrating that introducing the particle–mesh decomposition does not modify the equilibrium structure of the liquid.

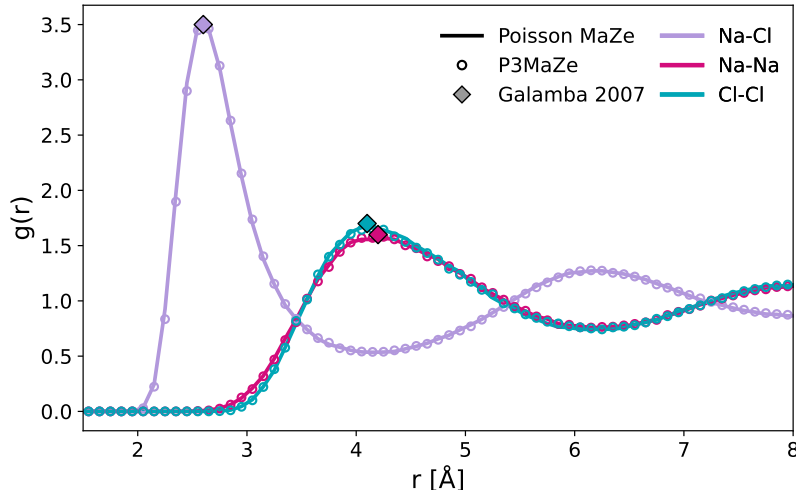


Figure 1: Partial radial distribution functions of molten NaCl obtained with Poisson MaZe and P3MaZe. The Na–Cl, Na–Na and Cl–Cl distributions are compared with the reference peak positions reported by Galamba *et al.* [37]. The two methods are in quantitative agreement, indicating that the particle–mesh decomposition preserves the equilibrium liquid structure.

Dynamical observables provide a more stringent validation because they accumulate the effect of the electrostatic forces over extended trajectories. We first examine the velocity autocorrelation function (VACF), from which the self-diffusion coefficients are obtained as

$$D_a = \frac{1}{3N_p} \sum_{\alpha=1}^{N_p} \int_0^{\infty} dt \langle \mathbf{v}_{\alpha}^a(t) \cdot \mathbf{v}_{\alpha}^a(0) \rangle, \quad (22)$$

where a denotes the ionic species and the average is taken over particles of that species and over time origins. Diffusion coefficients were estimated from ensembles of ten independent 15 ps microcanonical trajectories for each electrostatic method. Statistical uncertainties correspond to the standard error of the replica averages. Fig. 2 a) compares the normalized VACFs together with the cumulative diffusion coefficients. Agreement between Poisson MaZe and P3MaZe is observed over the entire correlation time, leading to statistically indistinguishable diffusion coefficients: $D_{\text{Na}} = (0.161 \pm 0.004) \times 10^{-3} \text{ cm}^2 \cdot \text{s}^{-1}$ and $D_{\text{Cl}} = (0.144 \pm 0.004) \times 10^{-3} \text{ cm}^2 \cdot \text{s}^{-1}$ for Poisson MaZe, compared with $D_{\text{Na}} = (0.159 \pm 0.004) \times 10^{-3} \text{ cm}^2 \cdot \text{s}^{-1}$ and $D_{\text{Cl}} = (0.146 \pm 0.004) \times 10^{-3} \text{ cm}^2 \cdot \text{s}^{-1}$ for P3MaZe. Both methods also agree with the reference values of Galamba *et al.* [37].

As a more demanding test, we next consider the current autocorrelation function (CACF), with the current computed as $\mathbf{J}(t) = \sum_{\alpha} Q_{\alpha} \mathbf{v}_{\alpha}(t)$. This correlation probes collective charge transport and is therefore particularly sensitive to the treatment of long-range electrostatic interactions [25]. The corresponding electrical conductivity was obtained from

$$\sigma_{\text{el}}(t) = \frac{1}{3Vk_{\text{B}}T} \int_0^t \langle \mathbf{J}(0) \cdot \mathbf{J}(t') \rangle dt', \quad (23)$$

using ensembles of twenty independent 40 ps trajectories. Fig. 2 b) shows that the current autocorrelation functions and cumulative conductivities obtained with Poisson MaZe and P3MaZe are statistically indistinguishable. The resulting conductivities, $\sigma_{\text{el}} = 4.29 \pm 0.15 \text{ } \Omega^{-1} \cdot \text{cm}^{-1}$ for Poisson MaZe and

$\sigma_{\text{el}} = 4.39 \pm 0.18 \text{ } \Omega^{-1} \cdot \text{cm}^{-1}$ for P3MaZe, are mutually consistent and remain close to the reference value reported by Mouhat *et al.* [38].

These structural and dynamical results demonstrate that introducing the particle–mesh decomposition into the MaZe framework leaves both equilibrium and transport properties unchanged within statistical uncertainty. The P3M decomposition therefore preserves the physical accuracy of the original constrained formulation while substantially reducing the computational cost of the long-range electrostatic treatment, as quantified in the following performance analysis.

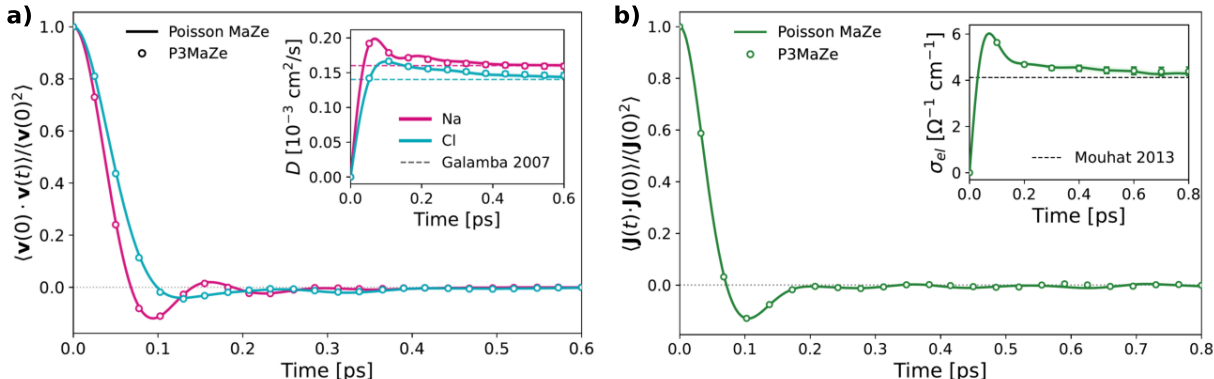


Figure 2: Comparison of single-particle and collective dynamical observables for molten NaCl obtained with Poisson MaZe and P3MaZe. **a)** VACF of Na^+ and Cl^- ions together with the corresponding cumulative Green–Kubo integrals used to determine the self-diffusion coefficients. **b)** CACF and cumulative Green–Kubo integrals yielding the electrical conductivity. Shaded regions indicate the standard error estimated from independent trajectories. The two methods produce statistically indistinguishable correlation functions and transport coefficients, demonstrating that introducing the particle–mesh decomposition into the MaZe framework preserves both single-particle and collective dynamical properties.

SPC/Fw model

Having established that P3MaZe reproduces the original Poisson MaZe formulation for a strongly ionic liquid, we consider a substantially more demanding benchmark based on the flexible SPC/Fw water model introduced by Wu, Tepper, and Voth [40]. Unlike molten salts, liquid water is not dominated by strong ionic correlations and high screening effects. Long-range electrostatic interactions instead play a central role in determining the hydrogen-bond network, molecular reorientation, and transport properties, making water a particularly sensitive test of the accuracy of the electrostatic treatment.

SPC/Fw is a flexible three-site model in which the interaction sites coincide with the atomic nuclei. Each water molecule is described by two O–H bond lengths and one H–O–H bond angle (all represented as harmonic interactions), allowing the intramolecular degrees of freedom to couple continuously to the electrostatic environment. The parameters of the model were taken from Ref. [40] and are summarized in the Supporting Information. As in the original SPC/Fw model, Lennard–Jones interactions act only on the oxygen site.

System and simulation protocol

In contrast with the molten-salt benchmark, where the comparison isolates the effect of introducing the particle–mesh decomposition into the MaZe framework, the SPC/Fw system assesses whether P3MaZe reproduces the structural and dynamical properties obtained with established particle–mesh electrostatic methods. The primary comparison is performed against the P3M implementation in LAMMPS through time-resolved structural and dynamical observables. As an additional consistency check, integrated observables are also compared with Ewald summation and the original Poisson MaZe formulation (Table 1).

The P3M and Ewald calculations were performed with LAMMPS, whereas P3MaZe and Poisson MaZe employed our in-house implementation. All four methods were applied to identical molecular configurations

and simulation conditions. The simulated system consists of 216 water molecules in a cubic periodic box of side $L = 18.552 \text{ \AA}$, corresponding to a density of $1.012 \text{ g} \cdot \text{cm}^{-3}$, at $T = 298.15 \text{ K}$. After a 1 ns equilibration in the canonical ensemble using a time step of 0.5 fs, production data were collected from forty independent 150 ps microcanonical trajectories. Initial configurations for the production runs were extracted every 500 ps from the equilibrated trajectory and used for all four electrostatic methods.

For the LAMMPS calculations, the real-space cutoff was 9.0 \AA , while the Ewald splitting parameter was determined automatically from the requested force accuracy of 10^{-7} , consistent with the original SPC/Fw parametrization [40]. The corresponding splitting parameter was then used to define the Gaussian width of the P3MaZe decomposition ($\sigma = 1.87 \text{ \AA}$). The real-space cutoff for P3MaZe was chosen from the convergence analysis reported in the Supporting Information, leading to $R_c = 6.0 \text{ \AA}$. A mesh of 40^3 grid points was found sufficient to converge all structural and dynamical observables discussed below. For Poisson MaZe, the electrostatic potential was represented on a uniform 180^3 mesh.

Observables

As mentioned above, the SPC/Fw benchmark assesses whether P3MaZe reproduces the structural and dynamical properties obtained with established particle–mesh electrostatic methods. We therefore compare time-resolved observables against the LAMMPS P3M implementation and summarize the corresponding integrated quantities for all four electrostatic methods (P3M, P3MaZe, Ewald, and Poisson MaZe) in Table 1. We first examine the equilibrium liquid structure through the oxygen–oxygen, oxygen–hydrogen, and hydrogen–hydrogen radial distribution functions. Fig. 3 compares the P3M and P3MaZe results together with the reference peak positions reported by Wu *et al.* [40]. The two methods are statistically indistinguishable over the full range of intermolecular separations, demonstrating that the P3MaZe particle–mesh decomposition preserves the equilibrium structure of liquid water.

As for the dynamical observables, we first consider the molecular VACF and the corresponding cumulative Green–Kubo integral for the self-diffusion coefficient. Fig. 4 a) shows that the normalized VACFs obtained with P3M and P3MaZe overlap over the entire correlation time, yielding nearly identical running diffusion coefficients and statistically indistinguishable plateau values. The corresponding numerical estimates are reported in Table 1, confirming that P3MaZe reproduces the translational dynamics of liquid water with the same accuracy as the standard P3M reference.

We next examine collective charge transport through the CACF and the corresponding cumulative electrical conductivity, shown in Fig. 4 b). Also in this case, P3MaZe reproduces the short-time decay, characteristic features of the correlation function and the cumulative conductivity obtained with P3M within the statistical uncertainty of the independent replicas. Because the cumulative conductivity exhibits residual long-time oscillations, the reported values are obtained by averaging over the plateau region and are summarized in Table 1. For the non-reactive SPC/Fw model, this quantity should not be interpreted as the experimental electrical conductivity of water, since autoionization and proton transport are absent. It nevertheless provides a sensitive probe of the long-range electrostatic correlations, in the same spirit as previous assessments of Coulomb solvers [25].

As a final dynamical validation, we consider rotational relaxation. Rotational correlation functions probe molecular reorientation and therefore complement the translational and collective transport observables discussed above. Fig. 5 reports the first- and second-order rotational correlation functions of the molecular dipole together with their cumulative relaxation times. The corresponding definitions are

$$C_1(t) = \langle P_1 [\mathbf{u}(t) \cdot \mathbf{u}(0)] \rangle = \langle \mathbf{u}(t) \cdot \mathbf{u}(0) \rangle \quad (24)$$

and

$$C_2(t) = \langle P_2 [\mathbf{u}(t) \cdot \mathbf{u}(0)] \rangle = \left\langle \frac{1}{2} \left(3 [\mathbf{u}(t) \cdot \mathbf{u}(0)]^2 - 1 \right) \right\rangle, \quad (25)$$

where \mathbf{u} is the molecular unit vector associated with the chosen axis. The main panel reports the correlation functions, while the inset shows the cumulative time integrals whose plateau values define the relaxation times τ_1 and τ_2 . Excellent agreement between P3M and P3MaZe is observed for both the correlation functions and the integrated relaxation times, indicating that the constrained particle–mesh formulation preserves the orientational dynamics of liquid water. The corresponding results for the H–H and O–H molecular axes are reported in the Supporting Information, while all integrated relaxation times are summarized in Table 1.

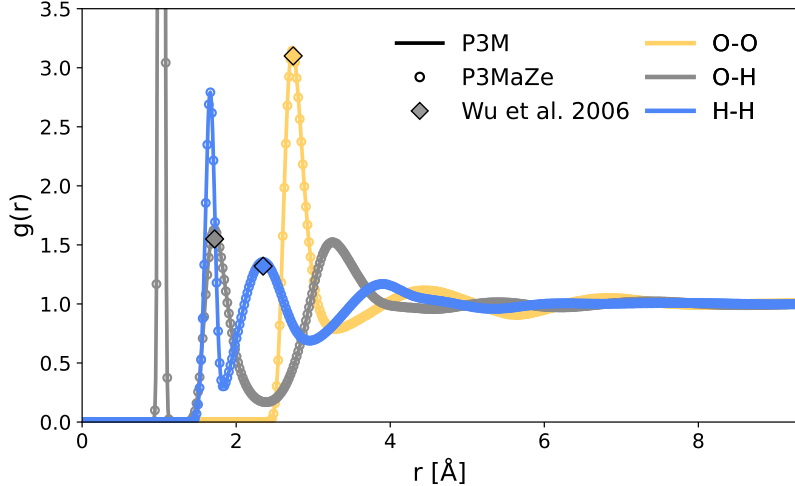


Figure 3: Comparison of oxygen–oxygen, oxygen–hydrogen and hydrogen–hydrogen radial distribution functions for SPC/Fw water obtained with P3M and P3MaZe. Diamond symbols indicate the reference peak positions reported by Wu *et al.* [40]. The agreement between the curves demonstrates that P3MaZe preserves the equilibrium structure of liquid water.

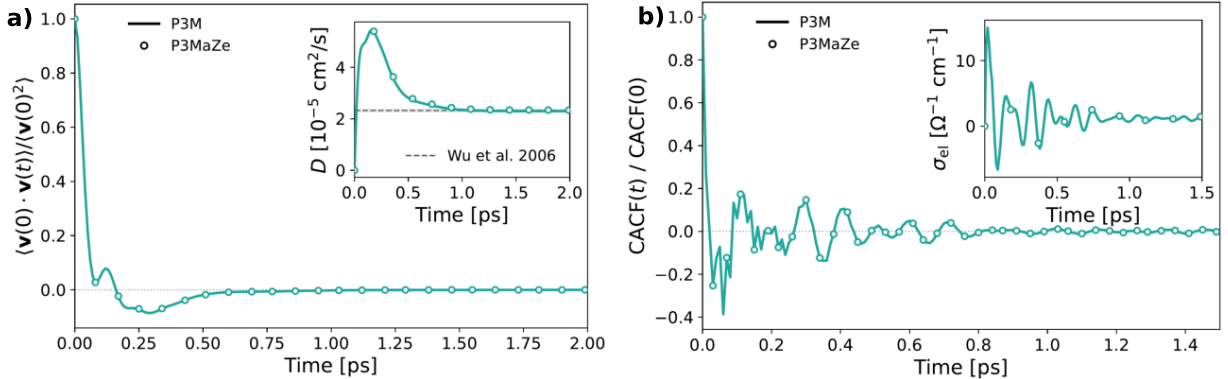


Figure 4: Comparison of single-particle and collective dynamical observables for SPC/Fw water obtained with P3M and P3MaZe. **a)** Normalized molecular VACF together with the cumulative Green–Kubo integrals used to determine the self-diffusion coefficient. **b)** Normalized CACF; the inset reports the cumulative electrical conductivity. The two methods produce statistically indistinguishable correlation functions and transport coefficients, demonstrating that the constrained particle–mesh formulation preserves both translational dynamics and collective electrostatic response.

The integrated observables for all four methods are collected in Table 1. P3M, P3MaZe, and Ewald yield mutually consistent estimates across all quantities, in good agreement with the reference values of Wu *et al.* [40]. Poisson MaZe, by contrast, systematically overestimates the self-diffusion coefficient and shows larger deviations in the rotational relaxation times, even at the high spatial resolution of $N = 180$ grid points per direction ($h = 0.103$ Å). This shows the sensitivity of Poisson MaZe to grid resolution in systems with weak ionic screening: unlike molten salts, liquid water presents a more demanding long-range electrostatic environment in which the full Coulomb grid problem converges more slowly with mesh refinement.

Taken together, these results indicate that P3MaZe preserves not only the structural properties of SPC/Fw water, but also both its single-particle and collective dynamical behavior.

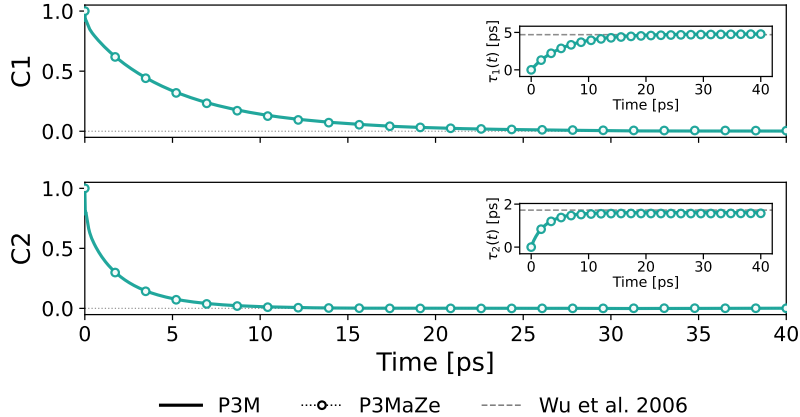


Figure 5: Comparison of dipole rotational relaxation in SPC/Fw water obtained with P3M and P3MaZe. The main panel reports the normalized first- and second-order rotational correlation functions, while the inset shows the corresponding cumulative relaxation times. Solid lines denote P3M and symbols denote P3MaZe. The close agreement between the two methods demonstrates that P3MaZe accurately reproduces the orientational dynamics of liquid water.

Table 1: Integrated structural and dynamical observables for SPC/Fw water obtained with P3M, P3MaZe, Ewald, and Poisson MaZe at 300 K. P3MaZe is statistically consistent with the established particle–mesh methods across all observables, while the comparison with Poisson MaZe highlights the improvement obtained by introducing the particle–mesh decomposition. Reference values are taken from Ref. [40], unless stated otherwise.

Observable	P3M	P3MaZe	Ewald	Poisson MaZe	Ref. value
D [10^{-5} cm ² /s]	2.29 ± 0.04	2.33 ± 0.04	2.30 ± 0.04	2.56 ± 0.05	2.32 ± 0.05
σ [Ω^{-1} /cm]	1.38 ± 0.04	1.40 ± 0.04	1.36 ± 0.05	1.30 ± 0.05	–
τ_1 (dipole) [ps]	4.88 ± 0.16	4.83 ± 0.14	4.88 ± 0.10	4.58 ± 0.10	4.70
τ_2 (dipole) [ps]	1.60 ± 0.04	1.58 ± 0.04	1.62 ± 0.04	1.51 ± 0.04	1.72
τ_1 (H–H) [ps]	4.70 ± 0.12	4.44 ± 0.10	4.49 ± 0.11	4.28 ± 0.10	3.90
τ_2 (H–H) [ps]	2.00 ± 0.04	1.98 ± 0.05	2.05 ± 0.05	1.95 ± 0.05	2.01
τ_1 (O–H) [ps]	4.79 ± 0.12	4.60 ± 0.12	4.52 ± 0.10	4.38 ± 0.10	4.17
τ_2 (O–H) [ps]	1.80 ± 0.04	1.81 ± 0.04	1.81 ± 0.04	1.75 ± 0.04	1.86

Performance and scaling

The objective of this part of the paper is to isolate the algorithmic consequences of replacing the conventional multigrid Poisson solver by the MaZe constrained formulation. To this end, we compare P3MaZe with both Poisson MaZe and an in-house real-space P3M implementation. The comparison with Poisson MaZe quantifies the effect of replacing the full real-space Poisson treatment by the short-range/long-range decomposition of P3MaZe. The comparison with the in-house P3M solver instead isolates the effect of introducing the MaZe correction mechanism at fixed long-range particle–mesh problem.

The in-house P3M implementation follows the same real-space multigrid structure as the Gaussian-based P3M approach of Sagui and Darden [26], with cubic B-splines used for charge assignment. It uses the same short-range/long-range splitting, smoothing procedure, simulation setup, numerical parameters, and Verlet prediction of the electrostatic potential for the multigrid iterations as P3MaZe, but replaces the constrained MaZe update by a conventional multigrid solution of the long-range Poisson equation. This provides a directly comparable reference for assessing how the constrained formulation affects solver convergence and overall cost. Fig. 6 compares the residual decay of the long-range electrostatic solvers as a function of the

number of multigrid iterations². For the MaZe-based methods, the monitored residual follows Ref. [35],

$$\text{res}_\nu = \max_n \left| \{ (M\mathbf{y}^\nu - \boldsymbol{\sigma}_p)_n \} \right|, \quad (26)$$

where \mathbf{y}^ν is proportional to the rescaled Lagrange multiplier after iteration ν , and $\boldsymbol{\sigma}_p$ is the constraint evaluated at the putative potential (Eq. (17)). In Poisson MaZe, this residual refers to the full discretized Poisson problem, whereas in P3MaZe it refers only to the smooth long-range constraint. For the in-house P3M solver, we monitor the maximum-norm residual of the direct multigrid solve,

$$\text{res}_\nu^{\text{P3M}} = \max_n \left| \left\{ \left(M\phi_{\text{LR}}^\nu + \frac{4\pi}{h} \mathbf{q}^s \right)_n \right\} \right|. \quad (27)$$

Although the P3M and P3MaZe residuals have different algebraic forms, they both measure convergence of the same long-range electrostatic equation.

The data in Fig. 6 were obtained from the same restart configurations used for the independent dynamical replicas. For each restart and each method, short trajectories of 100 MD steps were propagated, and the residual was recorded after each multigrid iteration during the field update. The initial steps of each trajectory were discarded because they are affected by the initialization of the field solver and converge more slowly than the subsequent plateau regime. The plotted curves therefore report the residual decay averaged over the remaining steps and over the restart configurations, while the shaded regions indicate the minimum-to-maximum spread across the analyzed samples.

In molten NaCl, Fig. 6 a), P3MaZe provides the fastest convergence. The prescribed tolerance is typically reached in one or two iterations, and always within one to four iterations over the sampled steps. By contrast, Poisson MaZe requires four to five iterations and the in-house real-space P3M solver requires five to six. This acceleration reflects the combined effect of the MaZe correction mechanism, discussed after Eq. (17), and the smoother long-range source term entering the P3MaZe constraint.

The SPC/Fw system provides a more demanding test of the constrained solver. All methods require more iterations than in molten NaCl, reflecting the weaker electrostatic screening of liquid water and the larger integration time step, both of which reduce the correlation between successive mesh updates. This system also allows us to assess different predictors for the Lagrange multipliers enforcing the Poisson constraint at time step $k + 1$. Three possibilities are considered. $\mathbf{y}_0^{(1)} = \mathbf{y}^k$, corresponding to the value of \mathbf{y} at the previous time step; $\mathbf{y}_0^{(2)} = 2\mathbf{y}^k - \mathbf{y}^{k-1}$, a Verlet-type extrapolation based on the two previous time steps; and $\mathbf{y}_0^{(3)} = 3\mathbf{y}^k - 3\mathbf{y}^{k-1} + \mathbf{y}^{k-2}$, a second-order extrapolation using three previous time steps. With the simplest predictor, $\mathbf{y}_0^{(1)}$, P3MaZe converges in approximately 13–14 iterations, already below the P3M baseline of 16–17 iterations. Poisson MaZe requires 17–19 iterations and therefore offers no convergence advantage over P3M for this weakly screened molecular system. Higher-order predictors substantially improve the P3MaZe convergence: $\mathbf{y}_0^{(2)}$ reduces the iteration count to approximately 11, while $\mathbf{y}_0^{(3)}$ further reduces it to 8–9, nearly halving the number of iterations relative to the direct real-space P3M solve. Whereas Fig. 6 characterizes the convergence of the iterative solve itself, Fig. 7 shows how this translates into the number of multigrid iterations required during molecular dynamics. In both systems, the first steps of the trajectory exhibit higher iteration counts before reaching a stable plateau. Across this plateau region, P3MaZe consistently requires fewer iterations than both P3M and Poisson MaZe, with the reduction further enhanced by higher-order predictors in SPC/Fw water. After characterizing solver convergence, we quantify how the reduced iteration count affects the overall computational cost. Fig. 8 reports the electrostatic CPU time per MD step as a function of system size on logarithmic axes for molten NaCl (panel a) and SPC/Fw water (panel b). The mesh resolution was scaled to preserve the mesh spacing h of the corresponding production simulations as N_p was increased. For each system, all simulations were performed at the same density. Linear fits in the log–log representation confirm the expected $\mathcal{O}(N)$ scaling of all real-space formulations, while the vertical offsets between the curves quantify the reduction in computational cost achieved by the different algorithms. For molten NaCl, Fig. 8 a), all methods exhibit approximately unit slopes, confirming the expected linear scaling of multigrid-based real-space particle–mesh electrostatics. Poisson MaZe is the most expensive

²For the multigrid solvers used here, one iteration corresponds to a single V-cycle: the residual is relaxed on the current grid, restricted to coarser grids, approximately corrected on the coarse levels, and then prolonged back to the fine grid with additional post-relaxation.

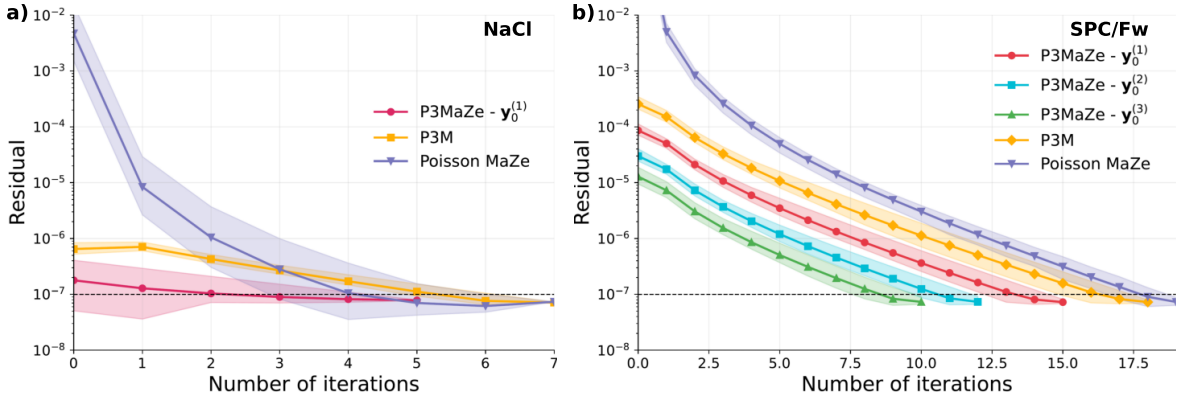


Figure 6: Residual convergence of the long-range electrostatic solver for a) molten NaCl and b) SPC/Fw water. Solid lines denote the mean residual decay, while shaded regions indicate the minimum-to-maximum spread over sampled MD steps and restart configurations. P3MaZe reaches the target residual in fewer multigrid iterations than the corresponding real-space P3M solver, with the advantage becoming particularly pronounced for SPC/Fw when higher-order predictors are used.

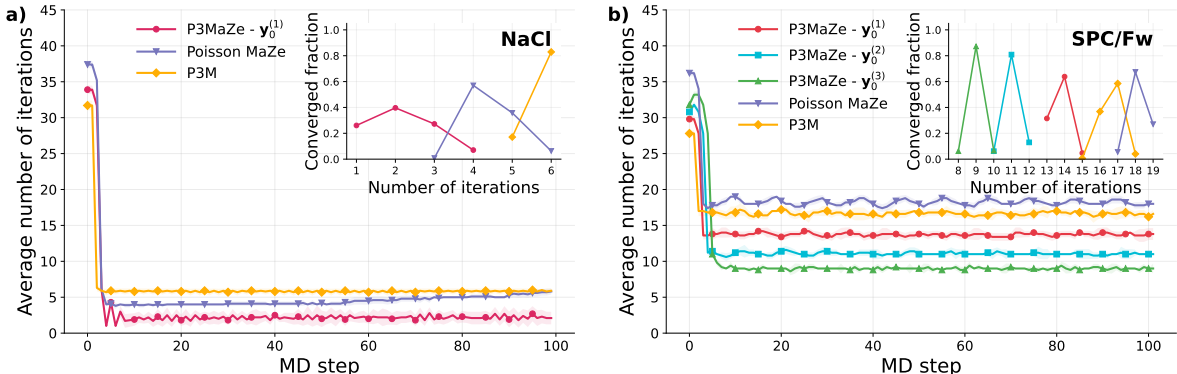


Figure 7: Average number of multigrid iterations per MD step for a) molten NaCl and b) SPC/Fw water. The inset in each panel reports the iteration-count distribution in the plateau regime. The faster residual convergence observed in Fig. 6 translates into a sustained reduction in the number of multigrid iterations during molecular dynamics, and higher-order predictors progressively improve the P3MaZe convergence in the more demanding SPC/Fw system.

method, with a fitted slope approximately 19 times larger than that of P3MaZe, reflecting the cost of solving the full Coulomb problem on the fine 120^3 reference grid. The in-house real-space P3M solver is approximately 2.8 times more expensive than P3MaZe, consistent with the larger number of iterations required by the direct Poisson solve. As the constrained formulation reduces the long-range solver cost, the smoothing step becomes the dominant contribution to the P3MaZe electrostatic time, accounting for approximately 50% of the total cost across the system sizes considered. The same linear scaling is observed for SPC/Fw water, Fig. 8 b). Here, Poisson MaZe is omitted because the fine mesh required for the full Coulomb grid problem makes it considerably expensive at the larger system sizes. The total electrostatic speedup of P3MaZe over P3M increases with the quality of the predictor, from approximately $1.1\times$ for $y_0^{(1)}$, to $1.4\times$ for $y_0^{(2)}$, and $1.6\times$ for $y_0^{(3)}$. These end-to-end gains are smaller than the solver-only reduction in iteration count because charge assignment and smoothing are identical across the compared methods and contribute a fixed preprocessing overhead. As a result, smoothing accounts for about 15% of the total electrostatic cost in P3M, but rises to 15–30% in the P3MaZe variants as the solver contribution decreases. These results show that the particle–mesh decomposition and the constrained-dynamics formulation act

synergistically. The decomposition reduces the dimensionality of the constrained electrostatic problem and smooths its source term, while the MaZe correction mechanism accelerates the long-range mesh update. The resulting method preserves the systematic accuracy controls of particle–mesh electrostatics while reducing the cost of the long-range solver. The timing analysis also identifies the next optimization target: once the multigrid correction is accelerated, particle–mesh preprocessing, and in particular the smoothing step, becomes the main remaining bottleneck.

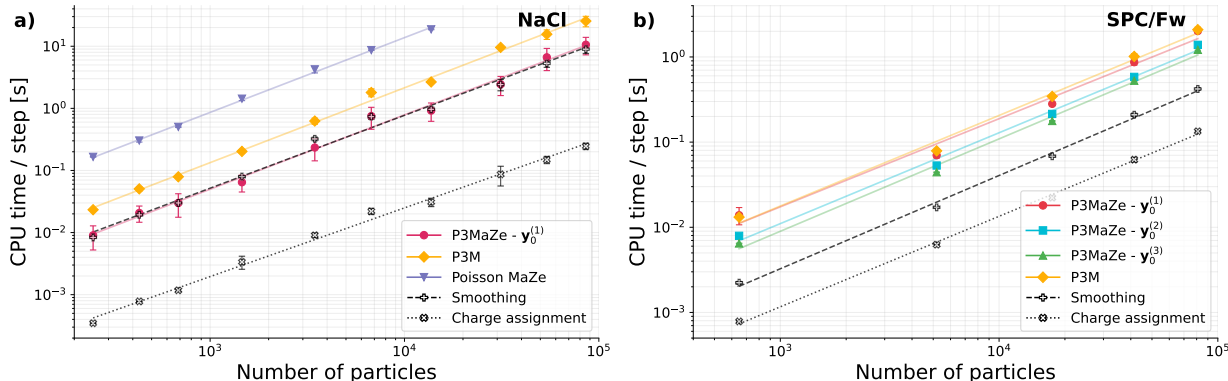


Figure 8: Electrostatic CPU time per MD step as a function of system size shown on logarithmic axes. Linear fits confirm the expected $\mathcal{O}(N)$ scaling of all real-space formulations, while the vertical separation between the curves quantifies the reduction in computational cost obtained with P3MaZe. Shared charge-assignment and smoothing costs are shown separately. **a)** Molten NaCl. **b)** SPC/Fw water.

Conclusions

We have introduced P3MaZe, a real-space particle–mesh electrostatic method that combines the standard short-range/long-range decomposition of P3M with the Mass-Zero constrained-dynamics framework. In this formulation, the smooth long-range electrostatic potential is treated as a zero-inertia auxiliary field whose evolution is constrained by the discretized Poisson equation. As a result, the long-range mesh problem is no longer solved through a conventional Poisson solve but through the constrained evolution of the auxiliary variables. This formulation combines the complementary strengths of particle–mesh electrostatics and constrained dynamics. By retaining the standard P3M decomposition, P3MaZe preserves the systematic accuracy controls associated with the real-space cutoff, the Ewald splitting, the mesh spacing, and the charge-assignment procedure. At the same time, the constrained formulation replaces the direct multigrid solution of the long-range Poisson equation by a correction problem that naturally exploits information from previous molecular dynamics steps to accelerate convergence.

The numerical benchmarks demonstrate that this reformulation preserves the physical accuracy of particle–mesh electrostatics. For molten NaCl, P3MaZe reproduces the structural and dynamical properties obtained with the original Poisson MaZe formulation and with literature reference data. For flexible SPC/Fw water, a substantially more demanding electrostatic benchmark, P3MaZe yields structural, translational, collective, and rotational dynamical observables that are statistically indistinguishable from those obtained with LAMMPS P3M and Ewald summation.

The solver analysis shows that the constrained formulation consistently reduces the cost of the long-range mesh solve. In both benchmark systems, P3MaZe requires fewer multigrid iterations than the corresponding real-space P3M solver, with higher-order predictors for the Lagrange multipliers providing additional gains in the more demanding SPC/Fw simulations. The timing analysis confirms that P3MaZe preserves the expected linear scaling of real-space particle–mesh electrostatics while reducing the prefactor associated with the long-range mesh solve. As the cost of the constrained long-range solve decreases, charge assignment and smoothing become an increasingly important fraction of the total electrostatic cost, identifying the particle–mesh preprocessing stage as the next target for algorithmic optimization.

These results establish P3MaZe as a controlled real-space formulation of particle–mesh electrostatics that preserves the systematic accuracy framework of P3M while introducing a fundamentally different strategy for solving the long-range mesh problem. The particle–mesh decomposition and the Mass-Zero constrained-dynamics framework act synergistically: the decomposition reduces the dimensionality of the constrained electrostatic problem and smooths its source term, while the constrained formulation accelerates the long-range mesh update. Beyond the immediate computational gains demonstrated here, this combination provides a flexible foundation for further algorithmic developments, including improved particle–mesh preprocessing, more effective predictor strategies, and implementations targeting highly parallel many-core and GPU architectures.

Acknowledgements

The authors thank Benoît Roux for seeding the idea of using MaZe for electrostatic calculations. This research was supported by the NCCR MARVEL, a National Centre for Competence in Research, funded by the Swiss National Science Foundation (grant number 205602).

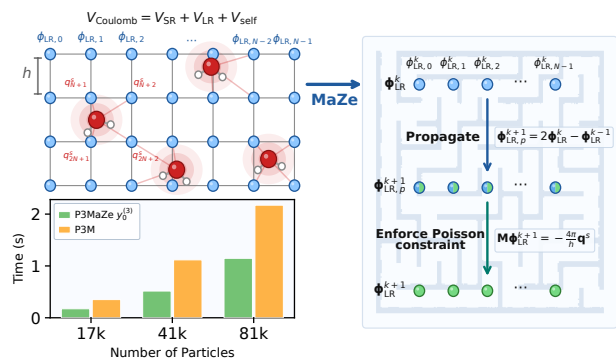
Supporting information

The supporting information contains the derivation of the P3MaZe equations of motion and their numerical integration scheme; convergence tests and tuning of the P3MaZe parameters; SPC/Fw force-field parameters; SPC/Fw rotational relaxation functions for the H–H and O–H bisectors; and numerical details of the performance scaling fits (Table S2).

References

- (1) Frenkel, D.; Smit, B., *Understanding molecular simulation: from algorithms to applications*; Elsevier: 2023.
- (2) Allen, M.; Tildesley, D., *Computer Simulation of Liquids*; Oxford Science Publications, Clarendon Press: Oxford, 1989.
- (3) Arnold, A.; Fahrenberger, F.; Holm, C.; Lenz, O.; Bolten, M.; Dachsel, H.; Halver, R.; Kabadshow, I.; Gähler, F.; Heber, F.; Iseringhausen, J.; Hofmann, M.; Pippig, M.; Potts, D.; Sutmann, G. *Physical Review E* **2013**, *88*, 063308.
- (4) George, A.; Mondal, S.; Purnaprajna, M.; Athri, P. *ACS Omega* **2022**, *7*, 32877–32896.
- (5) Ibeid, H.; Olson, L.; Gropp, W. *Journal of Parallel and Distributed Computing* **2020**, *136*, 63–74.
- (6) Ayala, A.; Tomov, S.; Stoyanov, M.; Haidar, A.; Dongarra, J. In *2022 IEEE International Parallel and Distributed Processing Symposium Workshops (IPDPSW)*, 2022, pp 372–381.
- (7) Simmonett, A. C.; Brooks, B. R. *The Journal of Chemical Physics* **2021**, *154*.
- (8) Zhou, Q.; Kousha, P.; Anthony, Q.; Shafie Khorassani, K.; Shafi, A.; Subramoni, H.; Panda, D. K. In *High Performance Computing*, ed. by Varbanescu, A.-L.; Bhatele, A.; Luszczek, P.; Marc, B., Springer International Publishing: Cham, 2022, pp 3–25.
- (9) Pollock, E.; Glosli, J. *Computer Physics Communications* **1996**, *95*, 93–110.
- (10) Ewald, P. P. *Annalen der physik* **1921**, *369*, 253–287.
- (11) Darden, T.; York, D.; Pedersen, L. *The Journal of Chemical Physics* **1993**, *98*, 10089–10092.
- (12) Essmann, U.; Perera, L.; Berkowitz, M. L.; Darden, T.; Lee, H.; Pedersen, L. G. *The Journal of Chemical Physics* **1995**, *103*, 8577–8593.
- (13) Hockney, R. W.; Eastwood, J. W., *Computer Simulation Using Particles*; McGraw-Hill: 1981.
- (14) Abraham, M. J.; Murtola, T.; Schulz, R.; Páll, S.; Smith, J. C.; Hess, B.; Lindahl, E. *SoftwareX* **2015**, *1–2*, 19–25.

- (15) Páll, S.; Zhmurov, A.; Bauer, P.; Abraham, M. J.; Lundborg, M.; Gray, A.; Hess, B.; Lindahl, E. *Journal of Chemical Physics* **2020**, *153*, 134110.
- (16) Phillips, J. C. et al. *Journal of Chemical Physics* **2020**, *153*, 044130.
- (17) Dehnen, W. *Journal of Computational Physics* **2002**, *179*, 27–42.
- (18) Gumerov, N. A.; Duraiswami, R., *Fast Multipole Methods for the Helmholtz Equation in Three Dimensions*; Elsevier: 2004.
- (19) Boateng, H. A. *Journal of Chemical Theory and Computation* **2019**, *16*, 7–17.
- (20) Skeel, R. D.; Tezcan, I.; Hardy, D. J. *Journal of Computational Chemistry* **2002**, *23*, 673–684.
- (21) Hardy, D. J.; Wu, Z.; Phillips, J. C.; Stone, J. E.; Skeel, R. D.; Schulten, K. *Journal of Chemical Theory and Computation* **2015**, *11*, 766–779.
- (22) Rossetto, V.; Maggs, A. C. *Physical Review Letters* **2002**, *88*, 196402.
- (23) Rottler, J.; Maggs, A. C. *Physical Review Letters* **2004**, *93*, 170201.
- (24) Fennell, C. J.; Gezelter, J. D. *The Journal of Chemical Physics* **2006**, *124*, 234104.
- (25) Beckers, J. V. L.; Lowe, C. P.; Leeuw, S. W. D. *Molecular Simulation* **1998**, *20*, 369–383.
- (26) Sagui, C.; Darden, T. *The Journal of Chemical Physics* **2001**, *114*, 6578–6591.
- (27) Sutmann, G.; Steffen, B. *Computer Physics Communications* **2005**, *169*, 343–346.
- (28) Ryckaert, J.-P.; Bellemans, A.; and, G. C. *Molecular Physics* **1981**, *44*, 979–996.
- (29) Coretti, A.; Bonella, S.; Ciccotti, G. *The Journal of Chemical Physics* **2018**, *149*, 191102.
- (30) Bonella, S.; Coretti, A.; Vuilleumier, R.; Ciccotti, G. *Physical Chemistry Chemical Physics* **2020**, *22*, 10775–10785.
- (31) Coretti, A.; Scalfi, L.; Bacon, C.; Rotenberg, B.; Vuilleumier, R.; Ciccotti, G.; Salanne, M.; Bonella, S. *The Journal of Chemical Physics* **2020**, *152*, 194701.
- (32) Girardier, D.; Coretti, A.; Ciccotti, G.; Bonella, S. *The European Physical Journal B* **2021**, *94*, 158.
- (33) Coretti, A.; Baird, T.; Vuilleumier, R.; Bonella, S. *The Journal of Chemical Physics* **2022**, *157*.
- (34) Angiolari, F.; Coretti, A.; Salanne, M.; Bonella, S. *Proceedings of the National Academy of Sciences* **2025**, *122*, e2520026122.
- (35) Troni, F.; Grassano, D.; Narayan, J.; Roux, B.; Bonella, S. *The Journal of Chemical Physics* **2025**, *163*, 214106.
- (36) Ryckaert, J.-P.; Ciccotti, G.; Berendsen, H. J. *Journal of Computational Physics* **1977**, *23*, 327–341.
- (37) Galamba, N.; Costa Cabral, B. J. *The Journal of Chemical Physics* **2007**, *126*, 124502.
- (38) F. Mouhat, S. B.; Pierleoni, C. *Molecular Physics* **2013**, *111*, 3651–3661.
- (39) Sivak, D. A.; Chodera, J. D.; Crooks, G. E. *The Journal of Physical Chemistry. B* **2013**, *118*, 6466–6474.
- (40) Wu, Y.; Tepper, H. L.; Voth, G. A. *The Journal of Chemical Physics* **2006**, *124*.



For Table of Contents Only

Supporting Information:

P3MaZe: A Mass-Zero constrained-dynamics formulation of particle–mesh electrostatics

Federica Troni,[†] Violette Gontran,[†] Davide Grassano,[†] and Sara Bonella^{*,†}

[†]*Centre Européen de Calcul Atomique et Moléculaire (CECAM), Ecole Polytechnique
Fédérale de Lausanne, 1015 Lausanne, Switzerland*

[‡]*National Centre for Computational Design and Discovery of Novel Materials (MARVEL),
Ecole Polytechnique Fédérale de Lausanne, CH-1015 Lausanne, Switzerland*

E-mail: sara.bonella@epfl.ch

1 P3MaZe evolution equations

We derive the Mass Zero equations of motion from the extended Lagrangian of Eq. (11) of the main text,

$$\begin{aligned} \mathcal{L}_{\text{P3MaZe}} = & \frac{1}{2} \sum_{\beta=1}^{N_p} m_{\beta} \dot{\mathbf{r}}_{\beta}^T \dot{\mathbf{r}}_{\beta} + \frac{1}{2} \mu \dot{\boldsymbol{\phi}}_{\text{LR}}^T \dot{\boldsymbol{\phi}}_{\text{LR}} \\ & - \bar{V}(\{\mathbf{r}_{\beta}\}) - V_{\text{SR}}(\{\mathbf{r}_{\beta}\}) - V_{\text{LR}}(\boldsymbol{\phi}_{\text{LR}}; \{\mathbf{r}_{\beta}\}) - V_{\text{self}} - \boldsymbol{\lambda}^T \boldsymbol{\sigma}_{\text{LR}}(\boldsymbol{\phi}_{\text{LR}}; \{\mathbf{r}_{\beta}\}), \end{aligned} \quad (1)$$

where μ is the fictitious inertia of the auxiliary degrees of freedom $\boldsymbol{\phi}_{\text{LR}}$, $\boldsymbol{\lambda}$ is the vector of Lagrange multipliers enforcing the constraint $\boldsymbol{\sigma}_{\text{LR}} = \mathbf{0}$ (Eq. (13) of the main text), V_{LR} is the discretized long-range electrostatic energy (Eq. (10) of the main text), and V_{self} is the, constant, Gaussian self-energy of Eq. (7) of the main text. The Euler–Lagrange equations

are

$$\begin{aligned}
m_\alpha \ddot{\mathbf{r}}_\alpha &= -\nabla_{\mathbf{r}_\alpha} V_{\text{SR}}(\{\mathbf{r}_\beta\}) - \nabla_{\mathbf{r}_\alpha} V_{\text{LR}}(\boldsymbol{\phi}_{\text{LR}}; \{\mathbf{r}_\beta\}) - \nabla_{\mathbf{r}_\alpha} \bar{V}(\{\mathbf{r}_\beta\}) \\
&\quad - \sum_n \lambda_n \nabla_{\mathbf{r}_\alpha} \sigma_{\text{LR},n}(\boldsymbol{\phi}_{\text{LR}}; \{\mathbf{r}_\beta\}), \\
\mu \ddot{\boldsymbol{\phi}}_{\text{LR},n} &= -\frac{\partial V_{\text{LR}}}{\partial \phi_{\text{LR},n}} - \sum_m \lambda_m \frac{\partial \sigma_{\text{LR},m}}{\partial \phi_{\text{LR},n}}.
\end{aligned} \tag{2}$$

Along the trajectory, the constraints

$$\sigma_{\text{LR},n} = \frac{\partial V_{\text{LR}}}{\partial \phi_{\text{LR},n}} = \left(\frac{h}{4\pi} \mathbf{M} \boldsymbol{\phi}_{\text{LR}} + \mathbf{q}^s \right)_n = 0. \tag{3}$$

are satisfied so the force term $-\partial V_{\text{LR}}/\partial \phi_{\text{LR},n}$ in the equation for the auxiliary variables is null. We also have $\frac{\partial \sigma_{\text{LR},m}}{\partial \phi_{\text{LR},n}} = M_{mn}$. Using the symmetry of the matrix \mathbf{M} and dividing and dividing by the inertia μ , we obtain for the evolution equation of the auxiliary variables

$$\ddot{\boldsymbol{\phi}}_{\text{LR}} = -\frac{h}{4\pi} \mathbf{M} \frac{\boldsymbol{\lambda}}{\mu}. \tag{4}$$

We now take the limit $\mu \rightarrow 0$. For $\ddot{\boldsymbol{\phi}}_{\text{LR}}$ to remain finite in this limit, we must have $\boldsymbol{\lambda} \rightarrow \mathbf{0}$ as $\mu \rightarrow 0$.^{S1,S2} We therefore define the rescaled multiplier $\boldsymbol{\eta} = \lim_{\mu \rightarrow 0} \frac{h}{4\pi} \boldsymbol{\lambda}/\mu$, which remains finite in the zero-inertia limit for the auxiliary variables. With this definition, we have

$$\ddot{\boldsymbol{\phi}}_{\text{LR}} = -\mathbf{M} \boldsymbol{\eta}. \tag{5}$$

Note that, for $\boldsymbol{\lambda} \rightarrow \mathbf{0}$, the constraint force term in Eq. (2) vanishes, and the equations of motion for the physical degrees of freedom reduce to

$$m_\alpha \ddot{\mathbf{r}}_\alpha = -\nabla_{\mathbf{r}_\alpha} V_{\text{SR}}(\{\mathbf{r}_\beta\}) - \nabla_{\mathbf{r}_\alpha} V_{\text{LR}}(\boldsymbol{\phi}_{\text{LR}}; \{\mathbf{r}_\beta\}) - \nabla_{\mathbf{r}_\alpha} \bar{V}(\{\mathbf{r}_\beta\}), \tag{6}$$

recovering exact physical dynamics and leading to Eq. (15) of the main text.

Numerical integration

The equations of motion above are integrated numerically using standard molecular dynamics algorithms.^{S1,S2} The physical degrees of freedom \mathbf{r}_α are evolved via velocity Verlet (or OVRVO for (N, V, T) simulations), while the auxiliary variables ϕ_{LR} are propagated via the standard Verlet algorithm,

$$\phi_{\text{LR}}^{k+1} = 2\phi_{\text{LR}}^k - \phi_{\text{LR}}^{k-1} - \frac{\Delta t^2}{2} \mathbf{M}\boldsymbol{\eta}, \quad (7)$$

where k denotes the time-step index and Δt is the timestep. Identifying the Verlet prediction $\phi_{\text{LR},p}^{k+1} = 2\phi_{\text{LR}}^k - \phi_{\text{LR}}^{k-1}$ as the provisional value, the time-updated field is

$$\phi_{\text{LR}}^{k+1} = \phi_{\text{LR},p}^{k+1} - \frac{\Delta t^2}{2} \mathbf{M}\boldsymbol{\eta}. \quad (8)$$

The rescaled Lagrange multipliers $\boldsymbol{\eta}$ are determined at each step by enforcing $\boldsymbol{\sigma}_{\text{LR}}(\phi_{\text{LR}}^{k+1}; \{\mathbf{r}_\alpha^{k+1}\}) = \mathbf{0}$. Substituting Eq. (8) into the constraint, we obtain

$$\frac{h}{4\pi} \mathbf{M}\phi_{\text{LR}}^{k+1} + \mathbf{q}^{s,k+1} = \mathbf{0} \implies \frac{h}{4\pi} \mathbf{M}\phi_{\text{LR},p}^{k+1} + \mathbf{q}^{s,k+1} = \frac{h}{4\pi} \Delta t^2 \mathbf{M}^2 \boldsymbol{\eta}. \quad (9)$$

Defining $\mathbf{y} = \frac{h}{4\pi} \frac{\Delta t^2}{2} \mathbf{M}\boldsymbol{\eta}$ so that $\mathbf{M}\mathbf{y} \stackrel{\text{def}}{=} \frac{h}{4\pi} \frac{\Delta t^2}{2} \mathbf{M}^2 \boldsymbol{\eta}$, and identifying the constraint residual at the putative potential as $\boldsymbol{\sigma}_{\text{LR},p}^{k+1} = \frac{h}{4\pi} \mathbf{M}\phi_{\text{LR},p}^{k+1} + \mathbf{q}^{s,k+1}$ (Eq. (17) of the main text), the above reduces to

$$\mathbf{M}\mathbf{y} = \boldsymbol{\sigma}_{\text{LR},p}^{k+1}, \quad (10)$$

which is the linear system of Eq. (16) of the main text. Once \mathbf{y} is obtained, the time-updated field follows as

$$\phi_{\text{LR}}^{k+1} = \phi_{\text{LR},p}^{k+1} - \frac{4\pi}{h} \mathbf{y}^*, \quad (11)$$

where \mathbf{y}^* is the solution of the linear system. This system is solved iteratively at each time step using the multigrid solver described in the main text.

2 Tuning of the P3MaZe parameters

The P3MaZe decomposition is controlled by the Gaussian screening width σ , the real-space cutoff R_c , and the number of mesh points per direction N . These parameters are coupled: narrower Gaussians require finer grids to resolve the screening charge density, but decay more rapidly in real space and therefore allow a smaller R_c .^{S3} The production parameters were selected from explicit convergence tests on the molten-salt system, using as reference a highly converged Poisson MaZe calculation on a grid with $N = 380$ points per direction. For fixed $\sigma = 1.39 \text{ \AA}$, the relative force error was computed for cutoffs in the range $R_c = 3.0\text{--}8.0 \text{ \AA}$ (in steps of 0.5 \AA). The error decreased monotonically with R_c and reached a plateau at approximately $R_c = 4.5 \text{ \AA}$, indicating that the residual error is no longer dominated by truncation of the short-range screened interaction. A convergence study in N at fixed σ and $R_c = 4.5 \text{ \AA}$ then showed that $N = 60$ ($h = 0.344 \text{ \AA}$) yields a relative force error of approximately 2.5% with respect to the reference at moderate computational cost. These values were adopted for production simulations. The same analysis was performed for simple point-charge flexible water (SPC/Fw) water model.

3 SPC/Fw parameters

Table adapted from.^{S4}

Table S1: SPC/Fw model parameters adopted in this work, taken from Ref.^{S4}

Parameter	Symbol	Value
Oxygen Lennard-Jones energy	ϵ_{OO}	0.1554253 kcal/mol
Oxygen Lennard-Jones size	σ_{OO}	3.165492 \AA
Oxygen charge	q_{O}	$-0.82 e$
Hydrogen charge	q_{H}	$+0.41 e$
Equilibrium O–H bond length	r_{OH}^0	1.012 \AA
Equilibrium H–O–H angle	θ_{HOH}^0	113.24°
Bond force constant	k_b	1059.162 kcal mol ⁻¹ \AA^{-2}
Angle force constant	k_a	75.90 kcal mol ⁻¹ rad ⁻²

4 SPC/Fw rotational relaxation time

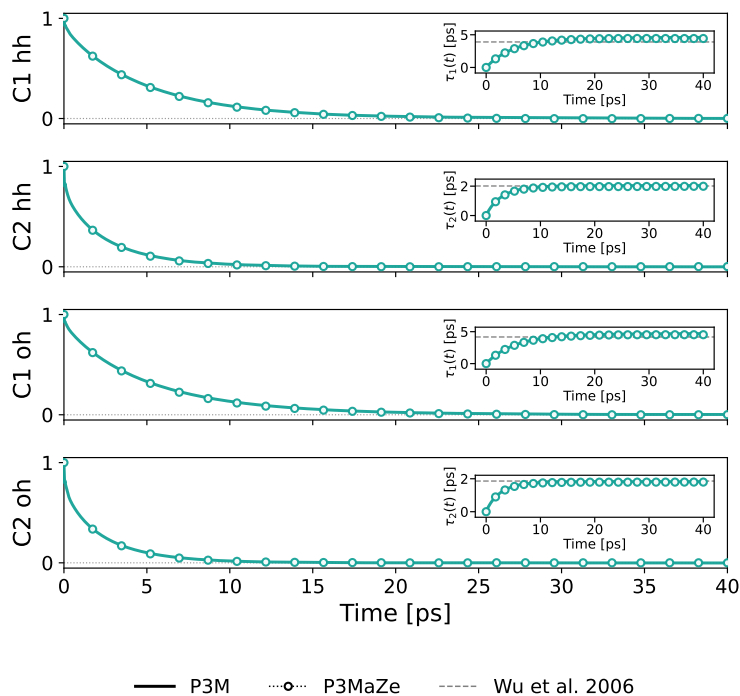


Figure S1: Comparison of rotational relaxation in SPC/Fw water for Particle-Particle Particle-Mesh and P3MaZe, considering only the HH and OH molecular bisectors. For each observable, the main panels report the ensemble-averaged first- and second-order rotational correlation functions, while the insets show the corresponding cumulative integral estimates of the relaxation times $\tau_1(t)$ and $\tau_2(t)$. The horizontal dashed lines mark the reference values from Wu *et al.*^{S4}

5 Performance fit Figure 8

Table S2 provides the full numerical details of the log-log linear fits underlying the performance analysis in the main text.

Table S2: Linear-fit slope a_{elec} of log-log total electrostatic CPU time per step vs. N_p , in units of s / step. The ratio $a_{\text{elec}}/a_{\text{elec}}^{\text{P3M}}$ quantifies the cost relative to our in-house P3M. The smoothing fraction reports the average percentage of the total electrostatic cost accounted for by the smoothing step, estimated from the timing data. Dashes indicate that a separate smoothing contribution is not defined for the method.

Method	a_{elec}	$a_{\text{elec}}/a_{\text{elec}}^{\text{P3M}}$	smoothing (%)
NaCl			
P3M	1.17×10^{-4}	1.00	27–34
P3MaZe	7.10×10^{-5}	0.61	47–57
Poisson MaZe	6.79×10^{-4}	5.81	–
SPC/Fw			
P3M	3.52×10^{-5}	1.00	14–16
P3MaZe $y_0 = y_0^{(1)}$	3.10×10^{-5}	0.88	16–20
P3MaZe $y_0 = y_0^{(2)}$	2.58×10^{-5}	0.73	19–25
P3MaZe $y_0 = y_0^{(3)}$	2.19×10^{-5}	0.62	23–26

The fitted slopes a_{elec} quantify the per-particle electrostatic cost in the large- N_p limit for each method and system. For SPC/Fw water, the cost ratios show a monotonic improvement from 0.88 for $y_0^{(1)}$ to 0.62 for $y_0^{(3)}$, with each successive predictor reducing the slope by roughly 0.13; the diminishing return suggests that the smoothing overhead, which grows from 16–20% to 23–26% of the total cost across the three variants, increasingly limits the benefit of further improving the initial guess.

References

- (S1) Coretti, A.; Bonella, S.; Ciccotti, G. Communication: Constrained molecular dynamics for polarizable models. *The Journal of Chemical Physics* **2018**, *149*, 191102.
- (S2) Troni, F.; Grassano, D.; Narayan, J.; Roux, B.; Bonella, S. Mass-zero constrained molecular dynamics for electrostatic interactions. *The Journal of Chemical Physics* **2025**, *163*, 214106.
- (S3) Sagui, C.; Darden, T. Multigrid methods for classical molecular dynamics simulations of biomolecules. *The Journal of Chemical Physics* **2001**, *114*, 6578–6591.

(S4) Wu, Y.; Tepper, H. L.; Voth, G. A. Flexible simple point-charge water model with improved liquid-state properties. *The Journal of Chemical Physics* **2006**, *124*.